

Flight Dynamics and Control Authority of Flap-Controlled Open Boxes

Eric Beyer*

Oregon State University, Corvallis, Oregon 97331

and

Mark Costello†

Georgia Institute of Technology, Atlanta, Georgia 30332

DOI: 10.2514/1.25301

The effectiveness of open-box micro air vehicles to deliver light, small payloads of high importance to specific ground coordinates is investigated through dynamic simulation. The open box exhibits interesting and varied flight dynamic behavior as key design parameters are changed. For example, the open box can achieve a coning behavior, a corkscrewing behavior, or glide much like a conventional aircraft to the ground by merely shifting the mass center location. The four rear flaps of the air vehicle can be used to control the box and affords the aircraft greater control authority than dispersion caused by typical atmospheric winds. This control mechanism can also be used as a braking system, which can greatly arrest the descent rate before ground impact. These dynamic qualities make the open box a promising airdrop vehicle which can cut through atmospheric winds towards the target before decelerating and gently landing.

Nomenclature

C_L, C_M, C_N	= aerodynamic moment coefficients in body reference frame
C_{LP}, C_{MQ}, C_{NR}	= aerodynamic damping moment coefficients in body reference frame
C_X, C_Y, C_Z	= aerodynamic force coefficients in body reference frame
D	= box reference diameter
$I_{xx}, I_{yy}, I_{zz}, I_{xy}, I_{xz}, I_{yz}$	= aircraft inertia matrix terms
L, M, N	= total applied moment components about mass center in body reference frame
p, q, r	= components of angular velocity vector in body reference frame
S	= box reference area
u, v, w	= components of velocity vector of mass center in body reference frame
u_A, v_A, w_A	= relative aerodynamic velocity components of mass center in body reference frame
V_A	= magnitude of relative aerodynamic velocity vector of mass center
V_{MW}	= magnitude of mean atmospheric wind
X, Y, Z	= total applied force components in body reference frame
x, y, z	= components of position vector of mass center in an inertial reference frame
$x_{p1 \rightarrow p2}^*, y_{p1 \rightarrow p2}^*, z_{p1 \rightarrow p2}^*$	= components of position vector from point $p1$ to $p2$ in body reference frame
α	= aerodynamic angle of attack
γ	= aerodynamic roll orientation

$\delta_1, \delta_2, \delta_3, \delta_4$	= flap deflection of flaps 1, 2, 3, and 4
ρ	= air density
ϕ, θ, ψ	= Euler roll, pitch, and yaw angles of box
ψ_{MW}	= azimuth angle of mean atmospheric wind

Introduction

MICRO air robots are small, autonomous, intelligent aircraft designed to focus on a specific task. The range of applications envisioned for future micro air robots in both the civilian and military sectors is quite wide [1,2]. Micro air robots promise to provide unparalleled situation awareness and data-gathering opportunities in many scenarios.

Future micro air robots are being designed in different shapes and sizes, and are being highly optimized to meet narrow mission specific requirements. Such unconventional configurations include the bioinspired flapping-wing, multirole morphing, and folding-wing, tube-launched micro air vehicles described by Jones [3], Abdulrahim [4], and Henry [5], respectively. The open-box micro air vehicle is another emerging configuration and is depicted in Fig. 1. These unpowered micro air vehicles are envisioned as cargo delivery platforms which are released from a parent aircraft operating at relatively high altitudes. Once released from the parent aircraft, the box settles into a steady-state condition. Subsequent to achieving a steady-state condition, an autonomous flight control system is activated to steer the system to specific ground coordinates. Control of the aircraft is achieved by independent deflection of the box flaps in the rear. All payload, actuators, sensors, batteries, and associated electronics are contained in the walls of the box. The air vehicle is designed with the mass center forward of the aerodynamic center so that the box falls to the ground in a stable fashion.

The work reported here investigates the basic flight mechanics of unpowered, controllable open-box aircraft configurations using simulations supported by wind-tunnel-obtained aerodynamic data. The basic modes of motion are reported as a function of mass configurations and typical flight behavior is documented. Using good mass management, the open box can achieve a stable gliding mode that can be autonomously controlled to deliver high-importance, small, light payloads. The rear flaps of the aircraft can also be used to dramatically arrest the rate of descent. Atmospheric wind dispersion is contrasted against control authority provided by flap deflection.

Presented as Paper 6326 at the AIAA Atmospheric Flight Mechanics Conference, Providence, RI, 16–19 August 2004; received 18 May 2006; revision received 25 October 2006; accepted for publication 30 November 2006. Copyright © 2006 by Mark Costello and Eric Beyer. Published by the American Institute of Aeronautics and Astronautics, Inc., with permission. Copies of this paper may be made for personal or internal use, on condition that the copier pay the \$10.00 per-copy fee to the Copyright Clearance Center, Inc., 222 Rosewood Drive, Danvers, MA 01923; include the code 0731-5090/07 \$10.00 in correspondence with the CCC.

*Graduate Research Assistant, Department of Mechanical Engineering, Member AIAA.

†Sikorsky Associate Professor, School of Aerospace Engineering, Associate Fellow AIAA.

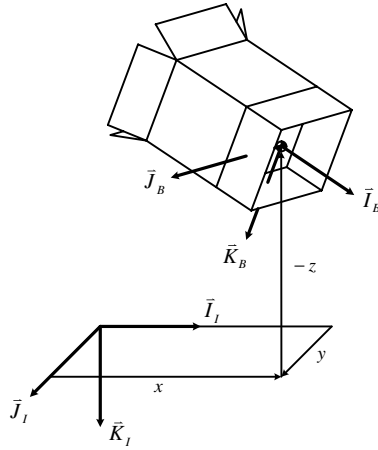


Fig. 1 Schematic of the open box with associated reference frames.

Box Dynamic Model

The numerical simulation employed in this study consists of a rigid-body, 6-DOF model typically used in flight dynamic modeling of air vehicles. A schematic of an open-box configuration with major elements of the system identified is given in Figs. 1 and 2. The degrees of freedom include three position components of the box mass center, as well as three Euler orientation angles of the body. The 12 equations of motion describing the flight dynamics of an open box are as follows:

$$\begin{Bmatrix} \dot{x} \\ \dot{y} \\ \dot{z} \end{Bmatrix} = \begin{bmatrix} c_\theta c_\psi & s_\phi s_\theta c_\psi - c_\phi s_\psi & c_\phi s_\theta c_\psi + s_\phi s_\psi \\ c_\theta s_\psi & s_\phi s_\theta s_\psi + c_\phi c_\psi & c_\phi s_\theta s_\psi - s_\phi c_\psi \\ -s_\theta & s_\phi c_\theta & c_\phi c_\theta \end{bmatrix} \begin{Bmatrix} u \\ v \\ w \end{Bmatrix} \quad (1)$$

$$\begin{Bmatrix} \dot{\phi} \\ \dot{\theta} \\ \dot{\psi} \end{Bmatrix} = \begin{bmatrix} 1 & s_\phi t_\theta & c_\phi t_\theta \\ 0 & c_\phi & -s_\phi \\ 0 & s_\phi/c_\theta & c_\phi/c_\theta \end{bmatrix} \begin{Bmatrix} p \\ q \\ r \end{Bmatrix} \quad (2)$$

$$\begin{Bmatrix} \dot{u} \\ \dot{v} \\ \dot{w} \end{Bmatrix} = \begin{Bmatrix} X/m \\ Y/m \\ Z/m \end{Bmatrix} - \begin{bmatrix} 0 & -r & q \\ r & 0 & -p \\ -q & p & 0 \end{bmatrix} \begin{Bmatrix} u \\ v \\ w \end{Bmatrix} \quad (3)$$

$$\begin{Bmatrix} \dot{p} \\ \dot{q} \\ \dot{r} \end{Bmatrix} = [I]^{-1} \begin{Bmatrix} L \\ M \\ N \end{Bmatrix} - \begin{bmatrix} 0 & -r & q \\ r & 0 & -p \\ -q & p & 0 \end{bmatrix} [I] \begin{Bmatrix} p \\ q \\ r \end{Bmatrix} \quad (4)$$

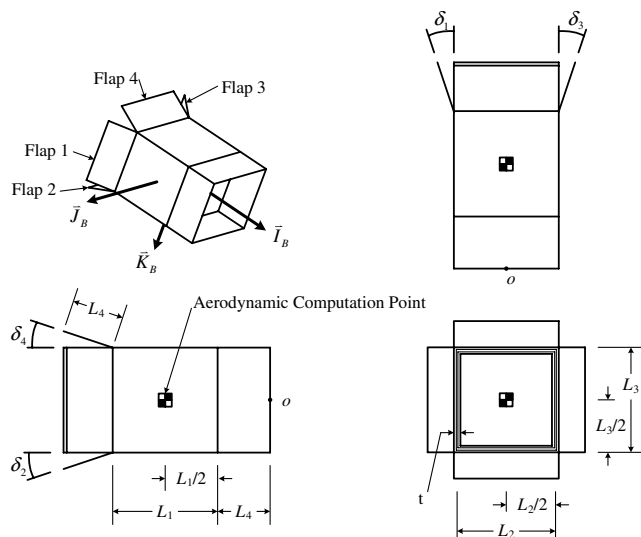


Fig. 2 Orthographic view of the open box with the dimensions and the location of the aerodynamic computation point.

where $[I]$ is the mass moment of inertia matrix of the box evaluated at the mass center with respect to body frame coordinates. The standard shorthand is used for trigonometric functions: $\cos(\alpha) \equiv c_\alpha$, $\sin(\alpha) \equiv s_\alpha$, and $\tan(\alpha) \equiv t_\alpha$. The applied loads contain contributions from weight W and air loads A .

$$\begin{Bmatrix} X \\ Y \\ Z \end{Bmatrix} = \begin{Bmatrix} X_W \\ Y_W \\ Z_W \end{Bmatrix} + \begin{Bmatrix} X_A \\ Y_A \\ Z_A \end{Bmatrix} = mg \begin{Bmatrix} -s_\theta \\ s_\phi c_\theta \\ c_\phi c_\theta \end{Bmatrix} + \frac{1}{2} \rho V_A^2 S \begin{Bmatrix} C_X \\ C_Y \\ C_Z \end{Bmatrix} \quad (5)$$

The aerodynamic forces are applied at the aerodynamic computation point, which is not necessarily the aerodynamic center. The applied moments about the box mass center contain contributions from two sources. Because the aerodynamic force given earlier is not located at the mass center, it produces a moment about the mass center. Also, because the computation point is not the aerodynamic center, an aerodynamic moment is also present. The applied moments about the box mass center is given by

$$\begin{Bmatrix} L_A \\ M_A \\ N_A \end{Bmatrix} = \frac{1}{2} \rho V_A^2 S D \begin{Bmatrix} C_L + \frac{pDC_{LP}}{2V_A} \\ C_M + \frac{qDC_{MQ}}{2V_A} \\ C_N + \frac{rDC_{NR}}{2V_A} \end{Bmatrix} + \begin{bmatrix} 0 & -z_{cg \rightarrow cp}^* & y_{cg \rightarrow cp}^* \\ z_{cg \rightarrow cp}^* & 0 & -x_{cg \rightarrow cp}^* \\ -y_{cg \rightarrow cp}^* & x_{cg \rightarrow cp}^* & 0 \end{bmatrix} \begin{Bmatrix} X_A \\ Y_A \\ Z_A \end{Bmatrix} \quad (6)$$

where $x_{cg \rightarrow cp}^*$, $y_{cg \rightarrow cp}^*$, and $z_{cg \rightarrow cp}^*$ are the components of the position vector from the center of mass to the aerodynamic computation point expressed in body frame coordinates.

The aerodynamic force and moment coefficients are dependent on aerodynamic angle of attack, aerodynamic roll orientation, and flap deflection. The magnitude of the aerodynamic angle of attack is given as

$$|\alpha| = \cos^{-1} \left(\frac{u_A}{\sqrt{u_A^2 + v_A^2 + w_A^2}} \right) \quad (7)$$

The angle of attack is defined as positive while w_A is positive and negative while w_A is negative. The aerodynamic roll orientation of the open box is defined as

$$\gamma = \tan^{-1} \left(\frac{v_A}{w_A} \right) \quad (8)$$

The relative aerodynamic velocity components of the box mass center used in the preceding equations are influenced by the atmospheric winds. The mean atmospheric wind acts in the horizontal ground plane and is directed at an angle ψ_{MW} from the I_I axis. Thus, the relative aerodynamic velocity components of the box mass center are

$$\begin{Bmatrix} u_A \\ v_A \\ w_A \end{Bmatrix} = \begin{Bmatrix} u \\ v \\ w \end{Bmatrix} - \begin{bmatrix} c_\theta c_\psi & c_\theta s_\psi & -s_\theta \\ s_\phi s_\theta c_\psi - c_\phi s_\psi & s_\phi s_\theta s_\psi + c_\phi c_\psi & s_\phi c_\theta \\ c_\phi s_\theta c_\psi + s_\phi s_\psi & c_\phi s_\theta s_\psi - s_\phi c_\psi & c_\phi c_\theta \end{bmatrix} \begin{Bmatrix} V_{MW} c_{\psi_{MW}} \\ V_{MW} s_{\psi_{MW}} \\ 0 \end{Bmatrix} \quad (9)$$

Aerodynamic Coefficient Determination

Limited public domain information is available for aerodynamic force and moment coefficient data for box shapes. Hoerner documents drag coefficient data for various square and rectangular 2-

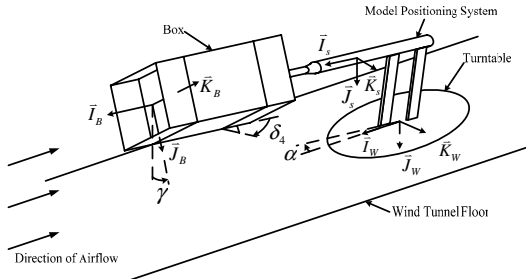


Fig. 3 Schematic of the open box mounted in wind tunnel.

D shapes, and cube and rectangular prism 3-D shapes [6]. Drag data are not provided as a function of angle of attack and sideslip. Hoerner and Borst provide limited data on normal force characteristics of square and cube shapes for different Reynolds numbers [7]. However, like the drag data, detailed information on lift as a function of angle of attack and sideslip are missing. Aerodynamic data were also found for missiles with square cross sections at various roll angles and angles of attack [8,9]. Unfortunately most of this work involved missiles with noses, fins, and aspect ratios larger than that of the open box considered here. Most of these missiles were tested at supersonic speeds and none allowed air to flow through them, unlike the open box. Other similar aerodynamics have been published on square section cantilever beams in smooth flow [10,11]. Aerodynamic force and moment data for box shapes with deflected flaps were not found in existing literature.

Thus, the aerodynamic coefficient data were experimentally obtained using a subsonic wind tunnel and a test model. The continuous flow, closed-circuit, low-speed wind tunnel located at Oregon State University has a test section area of 1.334×1.524 m and is capable of air speeds up to 20 m/s. A six-component sting balance is located in the middle of the test section and can be pitched and yawed using a model positioning system (see Fig. 3). The open box was mounted to the sting balance using a wire frame and hub assembly. The hub was designed to allow for rolling of the model. Once the box model was mounted to the sting, air was blown at the model while the forces and moments were tabulated for various angles of attack, roll orientations, and flap deflections. The air loads were then transformed from the sting frame to the body frame and the aerodynamic coefficients were computed as

$$\begin{Bmatrix} C_X \\ C_Y \\ C_Z \end{Bmatrix} = \frac{1}{2} \rho V_A^2 S \begin{Bmatrix} X_A \\ Y_A \\ Z_A \end{Bmatrix} \quad (10)$$

$$\begin{Bmatrix} C_L \\ C_M \\ C_N \end{Bmatrix} = \frac{1}{2} \rho V_A^2 S D \begin{Bmatrix} L_A \\ M_A \\ N_A \end{Bmatrix} \quad (11)$$

Because of symmetry of the open-box configuration with no flap deflection, a moderate set of angle variations covers many orientations. When a flap is deflected, aerodynamic symmetry of the box is largely lost and angle of attack and roll orientation must be varied through a larger set of angles. To generalize these

aerodynamic coefficients to the situation where several flaps are simultaneously deflected, superposition is used. By subtracting the aerodynamic coefficients calculated for the box with one flap deflected by that associated with no flap deflection, the contribution from one flap can be determined and generalized to each flap resulting in a model that predicts aerodynamic loads of a box with each flap deflected by a different amount.

The aerodynamic damping moment coefficients were approximated using two different means. The roll damping coefficient C_{LP} of the open box was assumed to be similar to that of a projectile of a bluff body. Such a projectile was found in PRODAS by Arrow Tech Associates and its roll damping coefficient was used for the open box. The pitch and yaw damping coefficients were approximated by considering a simple 2-D model for the box and calculating the moment produced when only two lifting surfaces are involved. Setting this moment equal to that of the standard aerodynamic damping moment produced the following equation:

$$C_{MQ} = C_{NR} = \frac{2(x_{cg \rightarrow cop}^*)^2}{D^2} C_{Z\alpha} \quad (12)$$

where $x_{cg \rightarrow cop}^*$ is the distance along I_B from the center of mass to the center of pressure and $C_{Z\alpha}$ is the slope of the normal force coefficient at small angles of attack and zero roll orientation.

Results

To investigate the flight dynamics and control authority of an open-box micro air vehicle, the equations of motion described in the preceding sections were numerically integrated using a fourth-order Runge–Kutta algorithm. The box used in this study was a triple-walled cardboard box with a mass of 345 grams (with no payload). The dimensions of the open box are shown in Fig. 2, in which $L_1 = 15.88$ cm, $L_2 = 15.56$ cm, $L_3 = 15.56$ cm, $L_4 = 7.94$ cm, and $t = 1.43$ cm. The mass center, roll inertia, and pitch inertia of the open box are 15.88 cm from the front of the box, 0.002834 kg · m², and 0.004312 kg · m², respectively. Because batteries, sensors, and other electronics are an integral part of any controllable micro air vehicle, additional mass was added to the box model, enabling the mass center to shift while changing the mass moment of inertia terms. The oversized wall thickness allows these electronic components to be imbedded into the walls of the box without disrupting the airflow through and around the aircraft. The mass properties (MP) and initial conditions (IC) used in this study are detailed in Tables 1 and 2, respectively. Only the upper flaps of the outer layer of the box are allowed to deflect, which creates a means of controlling the box while changing the flight dynamics.

Aerodynamic Force and Moment Coefficient Results

Aerodynamic coefficients of the open box were experimentally obtained using a wind tunnel and a full-scale test model of the open box. During testing, the air density varied between 1.16 and 1.22 kg/m³ while the air speed was maintained between 10 and 13 m/s. The roll orientation was varied from -90 to 90 deg in 15 deg increments and the angle of attack was varied between -60 and 60 deg. Because of the symmetry of the box, a limited amount of roll orientations and angles of attack can be used to determine other

Table 1 Mass properties of the featured open-box configurations

MP	1	2	3	4	5
Total mass, g	564.7	624.7	684.7	564.7	984.7
$x_{cg \rightarrow o}^*$, cm	9.69	8.76	7.99	9.69	5.56
$y_{cg \rightarrow o}^*$, cm	0.00	0.00	0.00	0.00	-2.54
$z_{cg \rightarrow o}^*$, cm	0.00	0.00	0.00	-3.05	-2.54
I_{xx} , kg · m ²	0.0046046	0.0050876	0.0055706	0.0040806	0.00671425
I_{yy} , kg · m ²	0.0085828	0.0093338	0.0099955	0.0085188	0.01190045
I_{zz} , kg · m ²	0.0085828	0.0093338	0.0099955	0.0081230	0.01190045
I_{xy} , kg · m ²	0.0000000	0.0000000	0.0000000	0.0000000	-0.00139034
I_{xz} , kg · m ²	0.0000000	0.0000000	0.0000000	-0.0016668	-0.00139034
I_{yz} , kg · m ²	0.0000000	0.0000000	0.0000000	0.0000000	0.00063568

Table 2 Initial conditions of the featured trajectories

IC	1	2	3
x_0 , m	0.0	0.0	0.0
y_0 , m	0.0	0.0	0.0
z_0 , m	Varied	Varied	Varied
ϕ_0 , deg	-5.0	0.0	35.0
θ_0 , deg	-60.0	-90.0	-12.0
ψ_0 , deg	15.0	0.0	20.0
u_0 , m/s	0.5	0.2	30.0
v_0 , m/s	-0.001	0.0001	2.0
w_0 , m/s	0.0002	-0.0002	-4.0
p_0 , rad/s	0.01	0.00001	1.0
q_0 , rad/s	0.1	0.004	3.0
r_0 , rad/s	0.002	-0.003	-1.5

orientations. Redundant data sets were taken and used to calculate an average load at those orientations. This helped rid any anomalies that may have existed with the mounting of the model or asymmetry in the model itself. The resulting aerodynamic coefficients expressed in the body frame as a function of the aerodynamic angle of attack and roll orientation are shown in Figs. 4–7 for the nominal open box with no flaps deflected. Note that the side force coefficient C_Y and the yawing moment coefficient C_N as a function of angle of attack and roll orientation are not reported because they can be determined from the plots of normal force and pitching moment coefficients, respectively. The reference surface area and reference diameter were defined as $L_2 \times L_3 = 242.04 \text{ cm}^2$ and $L_1 = 15.88 \text{ cm}$, respectively. The aerodynamic computation point was defined in the center of the box (see Fig. 2). It should also be noted that during simulation, aerodynamic coefficients associated with orientations not explicitly measured were estimated using a bilinear interpolation.

As is shown, the open box with no flap deflection has a maximum axial force magnitude when at 15-deg angle of attack, whereas the maximum side and normal force occurs when the angle of attack is between 40 and 50 deg for a given roll orientation. All three moment coefficients also reach a maximum at 40-deg angle of attack. The coefficient of drag and lift (C_{Drag} and C_{Lift}) were calculated as a function of angle of attack and roll orientation for the nominal no-flap deflection case. At 0-deg angle of attack the drag coefficient has a minimum value of 0.43, and it increases with larger angles of attack to a value between 3.1 (with $\gamma = 0 \text{ deg}$) and 4.0 (with $\gamma = 45 \text{ deg}$) at 60-deg angle of attack. The lift coefficient vs angle of attack curve is similar to that of symmetric airfoils with a lift slope of 0.1/deg while passing through $C_{\text{Lift}} = 0$ at 0-deg angle of attack. The stall angle of attack occurs at 40 deg with a $C_{\text{Lift(max)}}$ value that varies between 2.5 (with $\gamma = 0 \text{ deg}$) and 3.5 (with $\gamma = 45 \text{ deg}$) depending on the roll orientation. This large stall angle of attack and $C_{\text{Lift(max)}}$ is attributed to the large thickness of the box panels as well as it being a finite wing with a low aspect ratio [12,13].

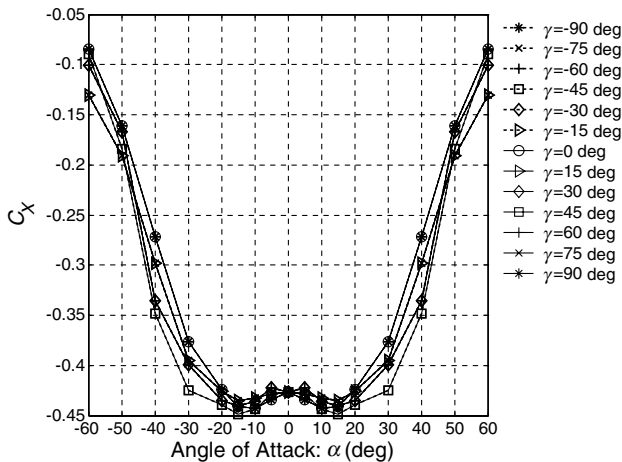


Fig. 4 Aerodynamic axial force coefficient as a function of the aerodynamic angle of attack and roll orientation ($\delta_1 = \delta_2 = \delta_3 = \delta_4 = 0 \text{ deg}$).

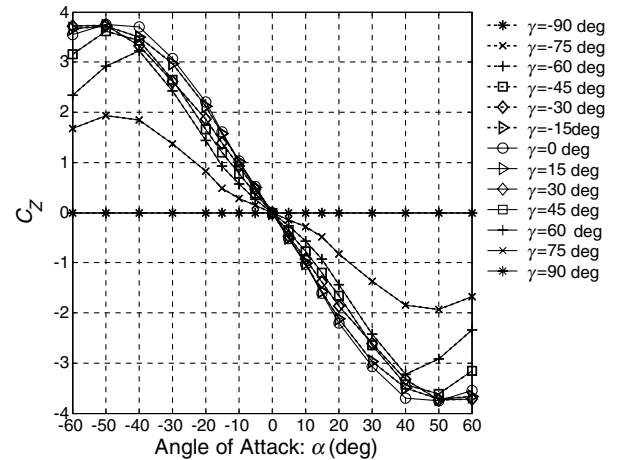


Fig. 5 Aerodynamic normal force coefficient as a function of the aerodynamic angle of attack and roll orientation ($\delta_1 = \delta_2 = \delta_3 = \delta_4 = 0 \text{ deg}$).

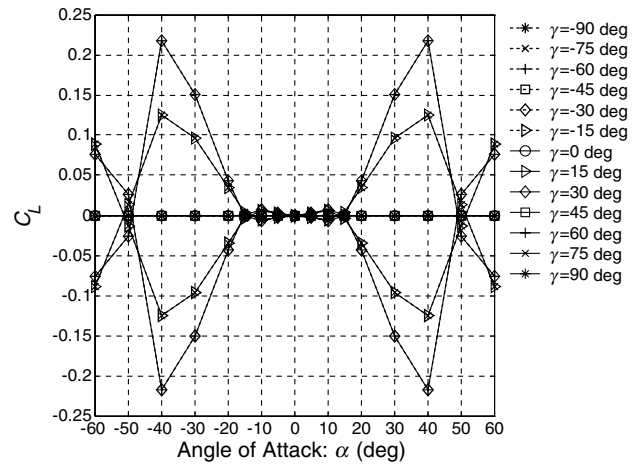


Fig. 6 Aerodynamic rolling moment coefficient as a function of the aerodynamic angle of attack and roll orientation ($\delta_1 = \delta_2 = \delta_3 = \delta_4 = 0 \text{ deg}$).

The same procedure for determining the aerodynamic coefficients was also performed while flap 4 was deflected by 10, 20, 30, 50, 70, and 90 deg. With the flap deflected, box symmetry was largely lost and the aerodynamic coefficients were altered. The magnitude of the axial force coefficient increases when a flap is deflected, whereas the normal force coefficient and the pitching moment coefficient become nonzero at 0-deg angle of attack. The coefficient of drag and lift vs

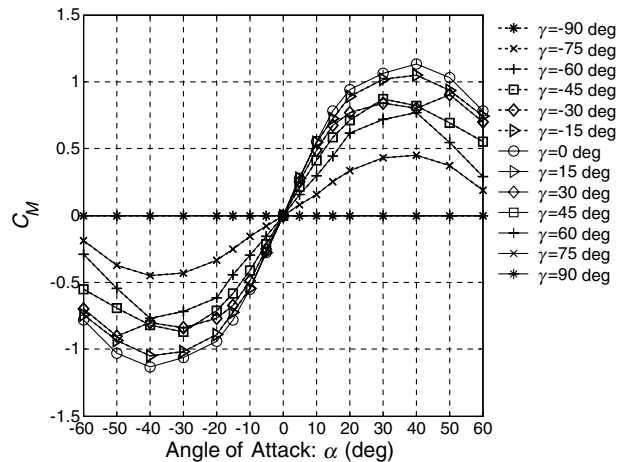


Fig. 7 Aerodynamic pitching moment coefficient as a function of the aerodynamic angle of attack and roll orientation ($\delta_1 = \delta_2 = \delta_3 = \delta_4 = 0 \text{ deg}$).

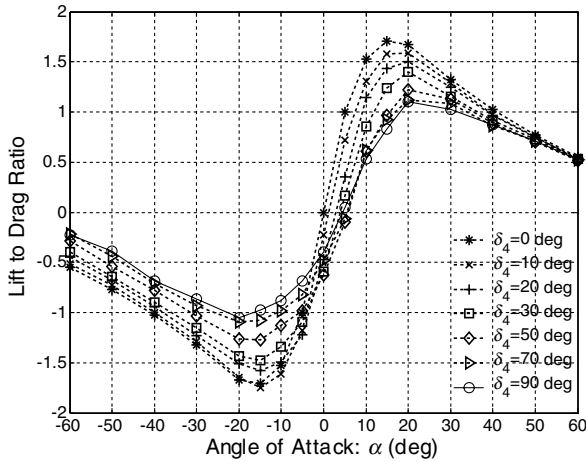


Fig. 8 Lift to drag ratio as a function of the aerodynamic angle of attack for various flap 4 deflections ($\gamma = 0$ deg).

angle of attack were calculated when flap 4 was deflected by the various amounts. Using this data, the lift to drag ratio was calculated as a function of angle of attack while the roll orientation was set to 0 deg and the results are plotted in Fig. 8. As shown, the best lift to drag ratio occurs with no flap deflection at an angle of attack of 15 deg with a value of 1.71. Increasing the flap deflection or the angle of attack past these values tends to decrease the lift to drag ratio. For a flap 4 deflection of 10, 20, 30, 50, 70, and 90 deg, the maximum lift to drag ratio occurs at 20-deg angle of attack with values of 1.59, 1.50, 1.40, 1.23, 1.12, and 1.10, respectively.

The roll damping coefficient was assumed to be -0.050 for all roll orientation and angles of attack. The pitch and yaw damping coefficients were calculated using Eq. (12) with $C_{Z\alpha} = -6.3$. The center of pressure location used in this equation was found by minimizing the pitching moment at low angles of attack and zero roll orientation. This center of pressure was found to exist at about 7.3 cm from the front of the box ($x_{cop \rightarrow o}^* \approx 7.3$ cm). Typical values for the pitch and yaw damping coefficients were between -0.011 and -0.613 depending on the location of the mass center.

Stability and Flight Dynamics

The stability of the open box can, to a certain extent, be determined by considering the longitudinal and roll static stability [13,14]. To understand longitudinal static stability, the aerodynamic pitching moment coefficient C_M vs angle of attack curve was examined about the mass center of the box. The open box possesses longitudinal static stability as long as the slope of this curve ($C_{M\alpha}$) is negative. An example of how the longitudinal static stability of the open box can change is given in Fig. 9 for a box with no flap deflection and at zero roll orientation. Here the center of mass was varied from the front of the box ($x_{cg \rightarrow o}^* = 0$ cm) to the center of the box ($x_{cg \rightarrow o}^* = 15.88$ cm) while keeping $y_{cg \rightarrow o}^*$ and $z_{cg \rightarrow o}^*$ equal to zero. As is shown, the open box possesses longitudinal static stability when the mass center is near the front of the box, becomes neutrally stable when $x_{cg \rightarrow o}^* \approx 7$ cm, and becomes unstable as the mass center approaches the center of the box. Also notice that only one equilibrium point is achieved when the center of mass is near the front of the box, but three equilibrium points exist when $x_{cg \rightarrow o}^*$ is between 7.3 and 12 cm. These curves can be shifted up or down by changing the amount of flap deflection or by varying $z_{cg \rightarrow o}^*$. Increasing the deflection of flap 4 will shift the curve up as will moving the center of mass in the K_B direction (increasing $z_{o \rightarrow cg}^*$). This allows the equilibrium point to exist at a higher angle of attack and increases the y intercept (C_{M0}).

For static roll stability, the slope of the aerodynamic roll moment coefficient C_L vs the roll orientation should be examined. Static roll stability is achieved if the slope of this curve ($C_{L\gamma}$) is negative. Although not shown, the plot of C_L vs roll orientation for various angles of attack is sinusoidal in nature with equilibrium points existing at $-90, -45, 0, 45,$ and 90 deg. The rolling moment coefficient is virtually zero for small angles of attack ($\alpha < 15$ deg)

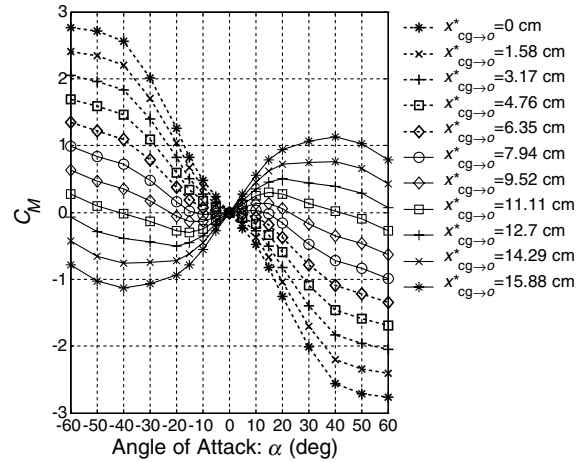


Fig. 9 Aerodynamic pitching moment coefficient as a function of the aerodynamic angle of attack for various $x_{cg \rightarrow o}^*$ positions ($y_{cg \rightarrow o}^* = z_{cg \rightarrow o}^* = 0$ cm, $\gamma = 0$ deg, $\delta_1 = \delta_2 = \delta_3 = \delta_4 = 0$ deg).

and reaches a maximum at an angle of attack of 40 deg. Various angles of attack and roll orientations allow the open box to exhibit unstable and stable static roll stability.

To better understand how the flight dynamics of the open box change for various mass center locations, three different mass configuration sets were considered during a parametric study. The first, case A, involved moving the center of mass along I_B while keeping it in the center of the box (J_B-K_B plane). The second mass configuration set, case B, allowed mass to accumulate along one of the front edges of the box so the mass center moved forward within the I_B-K_B plane. The last mass configuration set, case C, involved increasing the mass along two front edges of the box so the mass center shifted forward and toward one corner of the box. The flight behaviors associated with the different mass configurations are described in the following paragraphs as well as the dynamic stability of the system. To evaluate the dynamic stability of the open box, the equations of motion were numerically linearized about a steady-state condition [14,15]. The perturbations for angles were 0.0001 rad, 0.001 m/s for translational velocities, and 0.0001 rad/s for angular velocities.

The flight dynamics of the open box are greatly altered while shifting the mass center forward by evenly distributing mass along the front four edges of the box (case A). When the mass center is stationed further than approximately 11.0 cm from the front of the box ($x_{cg \rightarrow o}^* > 11$ cm and $y_{cg \rightarrow o}^* = z_{cg \rightarrow o}^* = 0$ cm), the box exhibits an unstable behavior and tumbles end over end until it impacts the ground, an expected result considering it is not longitudinally stable. If more weight is added to the front edges so the mass center lies between 9.2 cm $< x_{cg \rightarrow o}^* < 10.8$ cm, the box rolls and cones. An example of this behavior (MP 1, IC 1, and no atmospheric winds) is shown in Fig. 10, in which the line represents the location of the mass center and the box pictures depicts the orientation at different times along the trajectory. Note that only the last portion of the trajectory is shown so the steady-state condition can be examined. The box reaches a steady-state condition after approximately 60 s, which is characterized by the box rolling as it “cones” to the ground. The coning behavior can be described by defining a coning angle that is the angle between I_B and K_I . The coning angle oscillates at a frequency of 3.5 Hz at a value around 24.5 deg. This condition is associated with roll rate oscillations at 3.5 Hz between -11 and -11.8 rad/s, making the box roll one full revolution every 1.14 s. The forward velocity of the mass center reaches a maximum value of 16.65 m/s before decreasing to around 15.3 m/s due to the increased density of air at lower elevations. Although the forward velocity oscillates at a frequency of 3.5 Hz, the side and vertical velocity oscillate at only one quarter of this frequency at 0.875 Hz between ± 6.25 m/s. The pitch and yaw rate oscillate between ± 2.65 rad/s with a frequency of 0.875 Hz. The aerodynamic angle of attack maintains a value of around 22.4 deg with 3.5-Hz oscillations.

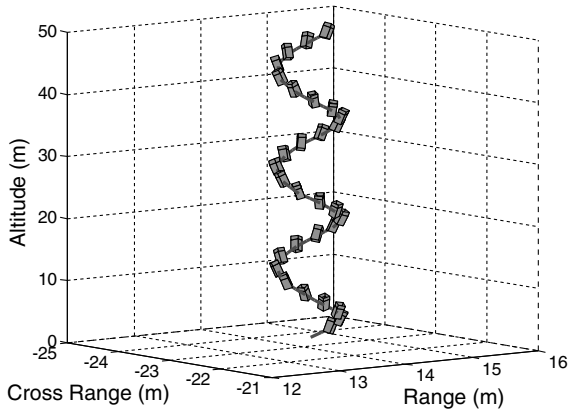


Fig. 10 Last section of trajectory for open box with MP 1, IC 1, and no atmospheric winds.

Once the mass center is brought between $8.7 \text{ cm} < x_{cg \rightarrow o}^* < 9.1 \text{ cm}$, the open box tends to glide. An example case was simulated with MP 2, IC 1, and no atmospheric winds. During steady state the rolling angle oscillates at a frequency of 0.6 Hz between 43.5 and 46.5 deg, the pitch angle oscillates around -12 deg , the roll rate oscillates between -0.1 and 0.1 rad/s , and the forward velocity decreases from 14.4 m/s to 13.25 m/s . The angle of attack oscillates around 18 deg while the roll orientation varies between 32 and 58 deg . The associated glide ratio (distance/altitude) was calculated to be approximately 1.7, which matches up well with lift to drag ratio at this particular angle of attack. This system possesses a neutrally stable pole associated with the body frame side and vertical velocity as well as the body roll rate. The mass configuration is neutrally stable when considering static roll stability, making it susceptible to wind gusts and other disturbances.

The open box flies in a “corkscrew” pattern if the mass center is brought between $7.7 \text{ cm} < x_{cg \rightarrow o}^* < 8.2 \text{ cm}$. The plot in Fig. 11 demonstrates this steady-state behavior for a box with MP 3, IC 1, and no atmospheric winds. Although this behavior looks much like that of the coning behavior of MP 1 and IC 1, the characteristics of the two trajectories are much different. The coning angle associated with the corkscrewing behavior does not oscillate like that of the previous. At steady state the coning angle remains fairly constant at 17.2 deg while the roll angle increases slowly due to a 4.1 rad/s roll rate. The forward velocity has increased to values of $25.7\text{--}23.5 \text{ m/s}$ due to the increased weight. The angle of attack maintains a value of 13.6 deg whereas the roll orientation is 22.6 deg . The eigenvalues associated with this corkscrewing behavior are shown in the root locus plot of Fig. 12. In this case, the mass of the box was increased from 668.7 to 708.7 g , which moved the mass center from $x_{cg \rightarrow o}^* = 8.18 \text{ cm}$ to $x_{cg \rightarrow o}^* = 7.72 \text{ cm}$. As is shown, these mass configurations are all stable. Two of the oscillatory modes are associated with the states u, v, w, q , and r . The higher oscillatory mode becomes more stable as weight is increased, whereas the other approaches the imaginary

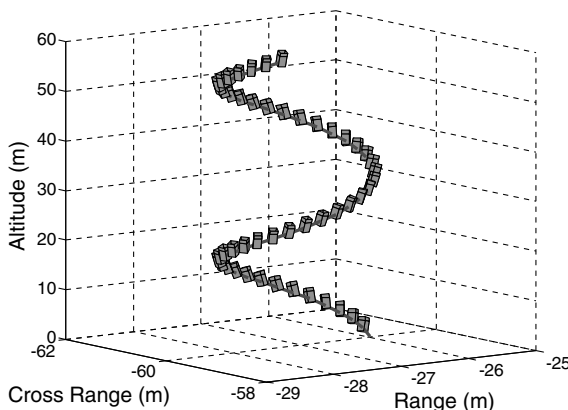


Fig. 11 Last section of trajectory for open box with MP 3, IC 1, and no atmospheric winds.

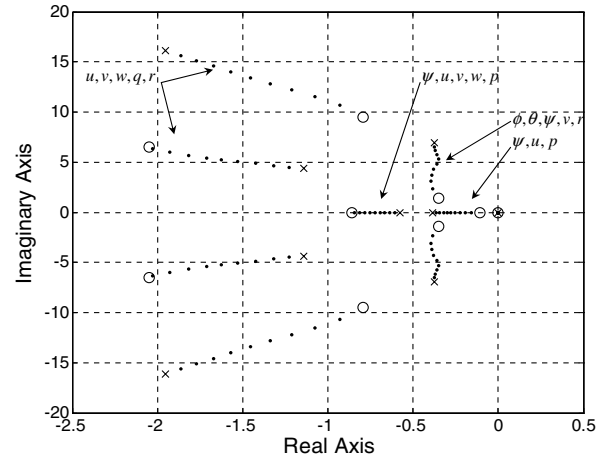


Fig. 12 Root locus of corkscrewing behavior for mass configurations of case A. (○: mass = 668.7 g; ×: mass = 708.7 g).

axis. The frequency of the third oscillatory mode associated with ϕ, θ, ψ, v , and r becomes greater as the center of mass is shifted forward. The mode associated with ψ, u, v, w , and p becomes less damped with increased weight, whereas the other mode associated with ψ, u , and p becomes more damped.

When more mass is added in the front of the box so the mass center lies between $6.94 \text{ cm} < x_{cg \rightarrow o}^* < 7.68 \text{ cm}$, the box becomes neutrally stable. This is explained in Fig. 9, in which the slope of $C_{M\alpha}$ is zero at the equilibrium point. If the mass is further increased so the mass center is positioned closer than 6.9 cm from the front of the box ($x_{cg \rightarrow o}^* < 6.9 \text{ cm}$), the box will reach a steady-state condition in which it falls straight down with 0-deg angle of attack. Once again, this behavior can be explained by noting that the slope of $C_{M\alpha}$ is negative (see Fig. 9) with an equilibrium point at 0-deg angle of attack.

Shifting the mass center towards a front edge of the box (case B) gives similar results as case A when the mass center is near the center of the box. The open box tends to display an unstable behavior by either tumbling or rolling and coning sideways. When more weight is added so the mass center lies between $r_{cg \rightarrow o} = 10.67I_B - 2.56K_B \text{ cm}$ and $r_{cg \rightarrow o} = 8.04I_B - 3.86K_B \text{ cm}$, the box tends to glide in a stable fashion with the weighted edge pointing towards the ground. This behavior is shown in the plot of Fig. 13 for MP 4, IC 1, and no atmospheric winds. The associated pitch angle is -7.8 deg , the roll rate is zero, and the forward velocity decreases with lower altitudes from 11.5 to 10.14 m/s . The angle of attack maintains a value of 27.3 deg during steady state and the associated glide ratio is approximately 1.42 as predicted by the lift to drag ratio at this angle of attack. Heavier boxes in this category shift the center of mass forward and downward, allowing for smaller steady-state angles of attack and hence greater glide ratios. A root locus plot of these mass configurations is given in Fig. 14, in which the mass has been increased from 512.7 to 683.7 g corresponding to the mass center varying from $r_{cg \rightarrow o} = 10.67I_B - 2.56K_B \text{ cm}$ to $r_{cg \rightarrow o} = 8.00I_B - 3.88K_B \text{ cm}$. As shown, an open box that is weighted with enough mass on one of the front edges is stable and has many of the same modes as a conventional aircraft. A rolling mode and a spiral mode associated with ϕ, ψ, v, p, r are shown to exist along the real axis. As more weight is increased, the rolling mode becomes more damped, whereas the spiral mode becomes less damped as it approaches the imaginary axis. Two longitudinal modes are also shown that involve the states θ, u, w, q . The frequency of the short period mode as well as the damping increases with increasing weight, whereas the Phugoid mode experiences less damping but about the same damped natural frequency. A Dutch roll mode is also shown associated with states ϕ, v, p, r . The eigenvalues of this mode become less stable as the center of mass is shifted forward and downward and the system eventually becomes unstable. This instability occurs for boxes that are weighted heavier than 682 g corresponding to mass center locations $x_{cg \rightarrow o}^* < 8.0 \text{ cm}$ and $z_{cg \rightarrow o}^* < -3.86 \text{ cm}$. These heavier boxes will tend to corkscrew towards the ground at high roll rates. It should also be

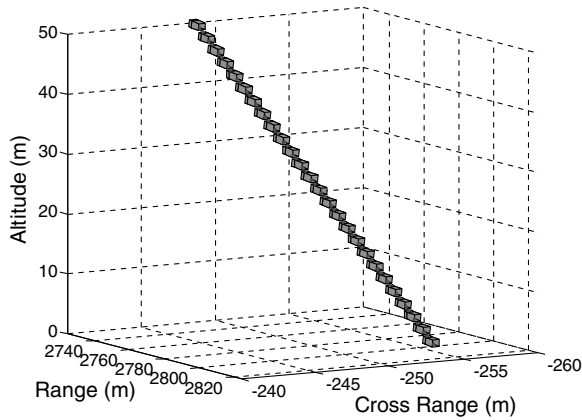


Fig. 13 Last section of trajectory for open box with MP 4, IC 1, and no atmospheric winds.

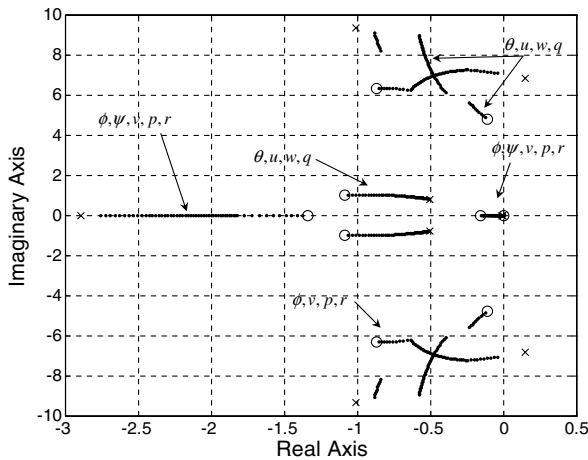


Fig. 14 Root locus of gliding behavior for mass configurations of case B. (O: mass = 512.7 g; x: mass = 683.7 g).

noted that the behavior of the mass configurations that glide well are dependent on initial conditions. These boxes may exhibit a coning behavior if extreme initial conditions are used.

The last mass configuration scheme, case C, involved increasing the mass along two adjacent edges of the box. With the mass center near the center of the box, the air vehicle will either tumble or roll and cone sideways. When more mass is added, the box rolls and cones down much like in case A. If the weight is further increased so the location of the mass center is between $r_{cg \rightarrow o} = 7.43I_B - 2.08J_B - 2.08K_B$ cm and $r_{cg \rightarrow o} = 6.64I_B - 2.28J_B - 2.28K_B$ cm, the open box glides like that of case A while gently rolling back and forth. Once again a neutrally stable pole exists for this mass configuration associated with the body frame side and vertical velocity as well as the body roll rate. The rolling motion dampens as the weight is further increased, allowing the box to glide with the weighted edge pointing towards the ground. Such a behavior occurs when MP 5, IC 1, and no atmospheric winds are simulated. The associated steady-state pitch angle is -26.6 deg, the forward velocity is about 25.6 m/s, and the roll rate is zero. The steady-state angle of attack is 8.0 deg, making the glide ratio about 1.45. Further increases in mass along the front edge result in decreased angles of attack and glide ratios.

Control Authority and Other Interesting Properties

Depending on the flight behavior of the open box during atmospheric flight, one might expect that the open box could cut through the air quite nicely while gliding, but be blown around by atmospheric wind while coning or corkscrewing. Average wind dispersion radii are given in Table 3, in which MP 1 and IC 2 were used. In this case, the open box was dropped at an altitude of 2000 m at various atmospheric wind speeds with an azimuth varying between

Table 3 Average dispersion radii of uncontrolled and controlled trajectories at an altitude of 2000 m

	MP	IC	Wind intensity, m/s	Average dispersion radius, m
Uncontrolled	1	2	2	266
Uncontrolled	1	2	4	414
Uncontrolled	1	2	8	941
Uncontrolled	4	3	2	273
Uncontrolled	4	3	4	582
Uncontrolled	4	3	8	1150
Controlled	4	3	0	1733

0 and 350 deg in 10 deg increments. Because the lightly weighted box falls relatively slowly while coning, the applied wind is able to push the box an average of 266, 414, and 941 m in a given direction with a 2, 4, and 8 m/s wind speed, respectively.

The potential to control an open box with weight along one of the front edges (case B) is great due to its conventional aircraft like flying characteristics and high glide ratio, which allows the box to achieve great control authority and cut through wind more effectively. Using the rear, outer flaps as control mechanisms, the open box can be guided in a given direction. A simple roll controller was implemented which deflected flap 1 or 3 by a small amount (<5 deg) depending on the direction of the roll rate so the maximum horizontal distance of the box could be achieved. When this controller was applied to a box with MP 4 and IC 3 with no mean atmospheric winds, the control authority radius was found to be approximately 1733 m. Note that the initial conditions represent those of a parent aircraft drop and that flap 4 was deflected by 30 deg to increase the stability of the system. Table 3 compares the average dispersion radii achieved by controlling the box with that of an uncontrolled box with the same mass properties and initial conditions but with applied atmospheric winds. The uncontrolled case has flap 1 deflected by 10 deg, which allows the box to corkscrew down while mean atmospheric winds of 2, 4, and 8 m/s in magnitude are applied, resulting in wind dispersion radii of 273, 582, and 1150 m, respectively. As is shown the control authority radius dominates the effect of wind on an uncontrolled open box.

Using the same simple roll controller, an open box weighted like case B can achieve greater control authority by applying additional mass to the front of the box or deflecting flap 4 by different amounts. Figure 15 demonstrates the control authority variation when controlling the open box while flap 4 is held at a constant angle ($\delta_4 = 30$ deg) but additional mass is added. Here the mass was varied from 521.7 to 746.7 g, which moved the mass center from $r_{cg \rightarrow o} = 10.49I_B - 2.65K_B$ cm to $r_{cg \rightarrow o} = 7.33I_B - 4.21K_B$ cm. As is shown, greater control authority can be achieved when the mass along the front edge of the box is increased to a certain point. This is because the steady-state angle of attack is decreased with heavier boxes, which moves the lift to drag ratio towards the maximum (see Fig. 8). The maximum lift to drag ratio for a flap deflection of 30 deg is 1.40, which occurs at 20-deg angle of attack. This is achieved when the mass is 731.7 g. Further increases in the mass result in smaller steady-state angles of attack and lowers the glide ratio as shown by the curve associated with a mass of 746.7 g in Fig. 15.

To achieve the maximum glide ratio for a specific flap deflection, the center of mass should be designed so the equilibrium point occurs at an angle of attack that corresponds to the maximum lift to drag ratio. Figure 16 shows the location of $x_{cg \rightarrow o}^*$ and $z_{cg \rightarrow o}^*$ for various flap 4 deflections to achieve the maximum lift to drag or glide ratio. Deviating from these mass center locations will tend to decrease the glide ratio. This is demonstrated by considering the points in Fig. 16 that represent the mass center location of the box configurations used earlier (and in Fig. 15). As is shown, increasing the weight moved the location of the mass center towards the optimum, which occurred when the mass was 731.7 g and then passed it resulting in a lower glide ratio.

Another interesting behavior of the open-box configuration is the ability to drastically reduce the rate of descent. Figure 17 shows the forward velocity of the box mass center as it falls from an altitude of

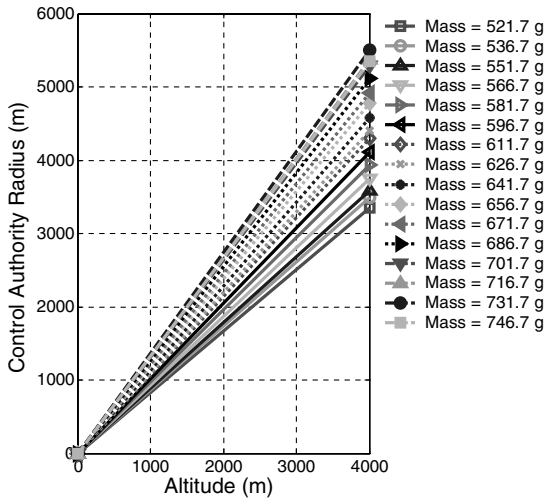


Fig. 15 Average control authority radius vs altitude for various mass configurations of case B with IC 2 and $\delta_4 = 30$ deg.

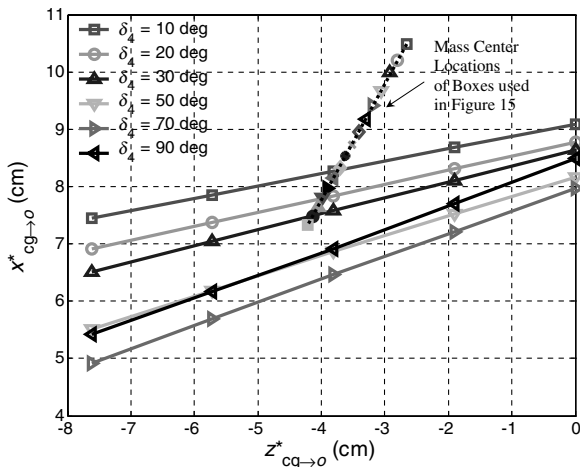


Fig. 16 $x^*_{cg \rightarrow o}$ vs $z^*_{cg \rightarrow o}$ for various δ_4 for maximum lift to drag ratio.

2000 m (MP 3, IC 1, and no atmospheric winds). At 40 s, all four rear flaps are deflected to 0, 20, 30, 50, 70, or 90 deg to increase the amount of drag. As is shown, with no flap deflection the open box achieves speeds up to 24 m/s and with more flap deflection the descent rate is arrested. When all the flaps are deflected by 90 deg, the descent rate is reduced to approximately half of the descent rate achieved with no flap deflection. This braking mechanism allows the open box to travel at relatively high speeds to avoid unwanted wind effects before slowing down before ground impact.

Conclusions

The open box is an emergent, unconventional micro air robot envisioned to carry small flat cargo to specific ground coordinates. The results presented show that the flight mechanics of the open box are largely dependent on the mass center location and are quite interesting, particularly the coning and corkscrewing behaviors. The aircraft also has the capability to glide like that of a conventional aircraft towards the ground in a stable manner. When the rear flaps are used as control mechanisms, this open-box configuration can achieve high glide ratios that more than overcome typical wind disturbances. This unique aircraft also has the ability to drastically arrest descent rate at crucial moments. All these dynamic qualities

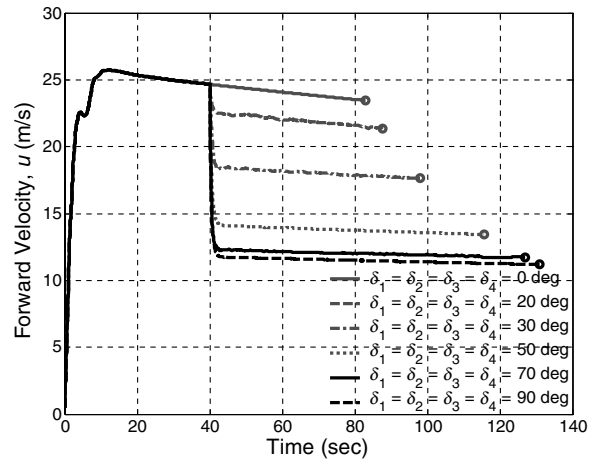


Fig. 17 Forward velocity of box mass center vs time for MP 3, IC 1, and no atmospheric winds from an altitude of 2000 m (all four flaps deflected at 40 s).

make the open box a promising airdrop vehicle that can travel at high speeds during most of the flight and avoid atmospheric wind effects that would normally create large dispersions such as for parafoils or parachutes. But at the same time, the open box has the ability to arrest impact velocity so fragile packages can be delivered.

References

- [1] Nordwall, B., "Micro Air Vehicles Hold Great Promise, Challenges," *Aviation Week and Space Technology*, Vol. 146, No. 15, April 1997, p. 67.
- [2] Mohan, S., and Sridharan, G., "Emerging Technologies for Micro-Unmanned Air Vehicles," *Defense Science Journal*, Vol. 51, No. 3, July 2001, pp. 223–228.
- [3] Jones, K. D., "Bio-Inspired Design of Flapping-Wing Micro Air Vehicles," *The Aeronautical Journal*, Vol. 109, No. 1098, Aug. 2005, pp. 385–393.
- [4] Abdulrahim, M., and Lind, R., "Control and Simulation of a Multi-Role Morphing Micro Air Vehicle," AIAA Paper 2006-6643, Aug. 2006.
- [5] Henry, J., "Design, Construction, and Testing of a Folding-Wing, Tube Launched Micro Air Vehicle," AIAA Paper 2005-1451, Jan. 2005.
- [6] Hoerner, S. F., *Fluid-Dynamic Drag*, Hoerner Fluid Dynamics, Bakersfield, CA, 1965.
- [7] Hoerner, S. F., and Borst, H. V., *Fluid-Dynamic Lift*, Hoerner Fluid Dynamics, Bakersfield, CA, 1975.
- [8] Daniel, D. C., Yechout, T. R., and Zollars, G. J., "Experimental Aerodynamic Characteristics of Missiles with Square Cross Sections," *Journal of Spacecraft and Rockets*, Vol. 19, No. 2, March–April 1982, pp. 167–172.
- [9] Sigal, A., and Lapidot, E., "Aerodynamic Characteristics of Configurations Having Bodies with Square, Rectangular, and Circular Cross Sections," *Journal of Spacecraft and Rockets*, Vol. 26, No. 2, March–April 1989, pp. 85–89.
- [10] Mukhopadhyay, V., and Dugundji, J., "Wind Excited Vibration of a Square Section Cantilever Beam in Smooth Flow," *Journal of Sound and Vibration*, Vol. 45, No. 3, April 1976, pp. 329–339.
- [11] Mukhopadhyay, V., "Gallop Oscillation of Square Section Suspended Cable in Smooth Flow," *Journal of Industrial Aerodynamics*, Vol. 5, No. 2, Oct. 1979, pp. 35–51.
- [12] Anderson, J. D., *Fundamentals of Aerodynamics*, McGraw-Hill, New York, 1991.
- [13] Dole, C. E., and Lewis, J. E., *Flight Theory and Aerodynamics: A Practical Guide for Operational Safety*, John Wiley & Sons, New York, 2000.
- [14] Nelson, R. C., *Flight Stability and Automatic Control*, McGraw-Hill, New York, 1989.
- [15] Rowell, D., and Wormley, D. N., *System Dynamics: An Introduction*, Prentice Hall, Upper Saddle River, NJ, 1997.